Environmental Chemistry and Ecotoxicology 7 (2025) 1671–1683

Contents lists available at ScienceDirect

Environmental Chemistry and Ecotoxicology

journal homepage: www.keaipublishing.com/en/journals/environmental-chemistry-and-ecotoxicology/

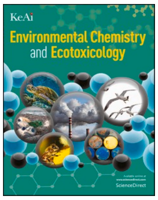

Research Paper

Unveiling the role of nitrogen-related functional groups in Imidacloprid adsorption by chitosan-modified graphitic biochar: A mechanistic insight into N-containing pollutant removal☆

Fuxiang Zhang [a,b,1], Jialin Lv [a,b,1], Fengyang Pan [a,b], Qiang Fu [a,b], Hongliang Jia [c], Yi-Fan Li [a,b,c], Rupert Hough [d], Zulin Zhang [d,a], Song Cui [a,b,*], Guorui Liu [e,*]

[a] International Joint Research Center for Persistent Toxic Substances (IJRC-PTS), School of Water Conservancy and Civil Engineering, Northeast Agricultural University, Harbin 150030, China
[b] Research Center for Eco-Environment Protection of Songhua River Basin, Northeast Agricultural University, Harbin 150030, China
[c] IJRC-PTS, College of Environmental Science and Engineering, Dalian Maritime University, Dalian, Liaoning 116026, China
[d] The James Hutton Institute, Craigiebuckler, Aberdeen AB15 8QH, UK
[e] Zhejiang Key Laboratory of Digital Intelligence Monitoring and Restoration of Watershed Environment, College of Geography and Environmental Sciences, Zhejiang Normal University, Jinhua 321004, China

ARTICLE INFO

Keywords:
Biochar
Chitosan
Nitrogen-doped biochar
Imidacloprid
Adsorption mechanisms

ABSTRACT

While significant progress has been made in the synthesis of nitrogen (N)-containing biochar, the fundamental mechanisms governing its interactions with N-containing pollutants, especially the role of N-related functional groups in adsorption processes, remain insufficiently explored. This study systematically investigates the adsorption behavior of imidacloprid (IMI), a representative N-containing pollutant, using a hierarchically structured N-doped graphitic biochar (NBC900) synthesized through a secondary pyrolysis approach. The optimized NBC900 exhibited an exceptional adsorption capacity of 140.1 $mg\cdot g^{-1}$ for IMI, achieving a removal efficiency of 97.2 %. The incorporation of chitosan as a nitrogen source and elevated pyrolysis temperature facilitated the formation of N-related functional groups and enhanced graphitization, which were critical for adsorption. NBC900 demonstrated excellent adaptability across a wide pH range (2–11), strong resistance to ionic strength variations, and remarkable reusability, highlighting its potential for practical applications. Comprehensive material characterizations revealed that the adsorption mechanism primarily involved chemisorption and π-π interactions, driven by the high degree of graphitization. Notably, the Lewis acid-base interactions between pyridine-N and carbonyl (C=O) groups on NBC900, as well as the nitro (-NO_2) and pyridine groups in IMI, provided novel insights into the adsorption mechanisms of N-containing pollutants. These findings establish a mechanistic framework for understanding of biochar's interaction with N-containing pollutants and offer a foundation for designing high-performance adsorbents for environmental remediation applications.

1. Introduction

Pharmaceutical compounds have been extensively utilized in agricultural production and human disease treatment [1,2]. However, their widespread use and continuous release into the environment have led to increased concentrations of these chemicals and their metabolites, resulting in significant water contamination [3–5]. Adsorption is widely recognized as a green remediation method for removing organic pollutants from water, with the adsorption mechanisms often elucidated through the examination of functional groups present in both adsorbents and pollutants [6,7]. Biochar, as a cost-effective and environmentally friendly biomass adsorbent, demonstrates significant potential due to its abundant availability and unique properties [8]. Produced through the pyrolysis of biomass under anoxic or anaerobic conditions, biochar

---

☆ This article is part of a Special issue entitled: 'Persistent toxic substances' published in Environmental Chemistry and Ecotoxicology.

* Corresponding authors at: International Joint Research Center for Persistent Toxic Substances (IJRC-PTS), School of Water Conservancy and Civil Engineering, Northeast Agricultural University, Harbin 150030, China.

E-mail addresses: cuisong-bq@neau.edu.cn (S. Cui), liiugr@zjnu.edu.cn (G. Liu).

[1] These authors contributed equally to this work.

https://doi.org/10.1016/j.enceco.2025.07.023
Received 14 June 2025; Received in revised form 26 July 2025; Accepted 29 July 2025

undergoes extensive aromatization and possesses ample surface functional groups, providing numerous sites for pollutant adsorption [9,10].

Recent research has focused on element doping to enhance the adsorption performance of biochar. Nitrogen (N), a ubiquitous element in nature, has been proposed for doping into biochar to increase the presence of N-related groups. The N atom, with its unpaired electrons, can elevate the electron density of adjacent carbon atoms and enhance electron mobility through sp2 conjugation, resulting in a greater abundance of functional groups and defect sites [11]. Additionally, N-doping can heighten the surface polarity of carbon materials, facilitating interactions with polar adsorbates [12]. These N-related groups not only serve as active sites for adsorbing organic pollutants [13,14] but also promote graphitization within the biochar structure, thereby enhancing its adsorption capacity. For example, Cheng et al. [13] synthesized N-doped biochars from cellulose and melamine through one-step pyrolysis at 1000 °C, achieving an enhanced atrazine adsorption capacity of 103.59 $mg \cdot g^{-1}$. This improvement was attributed to the increased specific surface area, higher degree of graphitization, and the presence of N-containing functional groups. Specifically, pyridinic-N and graphitic-N promoted adsorption through hydrophobic effects and π-π interactions, respectively, while pyrrolic-N and other surface functional groups (-COOH, -OH) facilitated hydrogen bonding. Similarly, Guy Laurent Zanli et al. [14] prepared cocoa shell-derived biochar using urea as a N source and sodium bicarbonate as an activator, achieving a high saturated adsorption capacity (134 $mg \cdot g^{-1}$) for norfloxacin. Their findings indicated that pore filling, hydrogen bonding, electrostatic interactions, and π-π interactions contributed to the adsorption mechanism, with graphitic-N and oxidized-N enhancing adsorption affinity by improving biochar conductivity. These studies demonstrate that N-doping can alter adsorption modes and enhance electron transfer, thereby improving adsorption capacity. However, detailed descriptions of the interaction mechanisms between N-groups in biochar and N-containing organic molecules remain limited.

Imidacloprid (IMI) is extensively applied in urban landscaping, pet treatments, forestry, and agricultural practices [1,4]. Structurally, IMI is a typical N-containing organic compound, featuring N-rich functional groups such as a nitroguanidine moiety and a chloropyridinyl ring, which confer upon it strong polarity and significant biological activity [15]. These characteristics, although advantageous for its pesticidal effectiveness, also result in high-water solubility and environmental persistence. As a result, a significant proportion of IMI enters natural water bodies through surface runoff and infiltration, leading to its widespread presence in global surface waters [16,17]. The increasing use of IMI in pet deworming and municipal greening programs has resulted in elevated concentrations in sewage treatment plants [18,19]. Conventional sewage treatment methods are often inefficient at removing IMI, leading to continuous pollution of surface water upon effluent discharge [17,18]. The environmental and health impacts of IMI have garnered significant attention, with epidemiological studies linking maternal exposure during pregnancy to higher incidences of anencephaly [20] and autism spectrum disorders [21]. These findings highlight IMI not only as a pesticide but also as a contaminant requiring immediate attention [5,22]. The persistent presence of IMI in aquatic environments underscore the urgent need for innovative, efficient, and sustainable approaches to mitigate its impact on ecological and human health.

Adsorption has been extensively investigated for IMI removal due to its selectivity, operational simplicity, low cost, and absence of byproducts [23]. The adsorption mechanism of biochar for IMI involves various interactions, including hydrophobic interactions, pore filling, hydrogen bonding, electrostatic interactions, and π-π interactions [3,24,25]. Physical adsorption, dominated by pore filling, and hydrogen bonding and electrostatic interactions facilitated by biochar's porous structure and charge attraction, play significant roles [3,26]. However, desorption can occur with changes in environmental conditions, highlighting the importance of electron transfer and group bonding processes for stable pollutant adsorption [14,27]. A deeper understanding of these bonding processes is crucial for the efficient removal of organic pollutants from water.

Given the limited research on the adsorption mechanisms of N-containing pollutants, this study aims to: (1) prepare and characterize N-doped graphitic biochar (NBC); (2) investigate the adsorption performance and evaluate influencing factors for the removal of IMI from aqueous solutions; and (3) elucidate the intricate interactions between NBC and IMI. This research will provide critical insights into the adsorption mechanism of IMI, advancing water treatment technologies and mitigating human exposure risks.

2. Materials and methods

2.1. Chemicals and sorbents

All chemicals used in this study were of analytical grade and were employed without further purification, as detailed in the Supporting Information (**SI**, **Text S1**). White melon seed shell biochar (WBC) was selected as the carbon-based material because our previous study (Cui et al. [27]) demonstrated its favorable adsorption performance and well-developed pore structure. Chitosan was primarily introduced as a N source. As a naturally abundant gel-like material, chitosan undergoes cross-linking under alkaline conditions to form insoluble hydrogels, which develop into a porous, network-like structure upon drying. This characteristic facilitates a more uniform modification of the biochar matrix and enhances the distribution of N functionalities. WBC and chitosan were mixed in a 1:1 mass ratio to prepare the precursor composite. Specifically, 1 g chitosan was uniformly dispersed in 50 mL of acetic acid solution (2.5 % *v*/v) and stirred in a water bath at 40 °C for 30 min to ensure complete dissolution. Subsequently, the pre-weighed WBC was added to the chitosan-acetic acid solution, and the mixture was subjected to hydrothermal treatment for an additional 30 min. Following this, 20 mL of NaOH solution (2 $mol \cdot L^{-1}$) was slowly added to the mixture under continuous magnetic stirring for 2 h. The resulting precipitate was filtered, rinsed thoroughly, and dried at 85 °C. Finally, the dried composite was pyrolyzed twice at temperatures of 500 °C, 700 °C, and 900 °C to produce N-doped graphitic biochar, designated as NBC-X, where X represents the pyrolysis temperature. The highest pyrolysis temperature of 900 °C was selected based on our previous research (Cui et al. [27]), which demonstrated that WBC prepared at this temperature possesses a larger specific surface area and total pore volume, thereby significantly enhancing its adsorption performance.

2.2. Characterization

The physicochemical properties of the synthesized materials were characterized using the following techniques: elemental analyzer (EA, Elementar Analyzer, Unicube, Germany), Scanning Electron Microscopy (SEM, ZEISS GeminiSEM 300, Germany), Energy-dispersive spectroscopy (EDS, ZEISS GeminiSEM 300, Germany), Brunauer-Emmett-Teller (BET) surface area analysis (Micromeritics ASAP 2460, USA), X-ray photoelectron spectroscopy (XPS, Thermo Scientific K-Alpha, USA), Fourier transform infrared spectroscopy (FTIR, Thermo Nicolet 370, USA), X-ray diffraction (XRD, Bruker D8 Advance, Germany), and Raman spectroscopy (Renishaw inVia Raman Microscope, UK). Detailed methodologies for these techniques are provided in **Text S2**.

2.3. Adsorption experiments: Isotherms, kinetics, and water chemistry

Adsorption isotherms and Kinetics were employed to evaluate the adsorption capacity and mechanisms of NBC for IMI. The detailed calculation formulas are provided in **Text S3**. Batch adsorption experiments were conducted by adding 40 mg of adsorbent to 40 mL of IMI solution at varying concentrations in centrifuge tubes. The mixtures were shaken at 200 rpm for different durations (5–1440 min) at

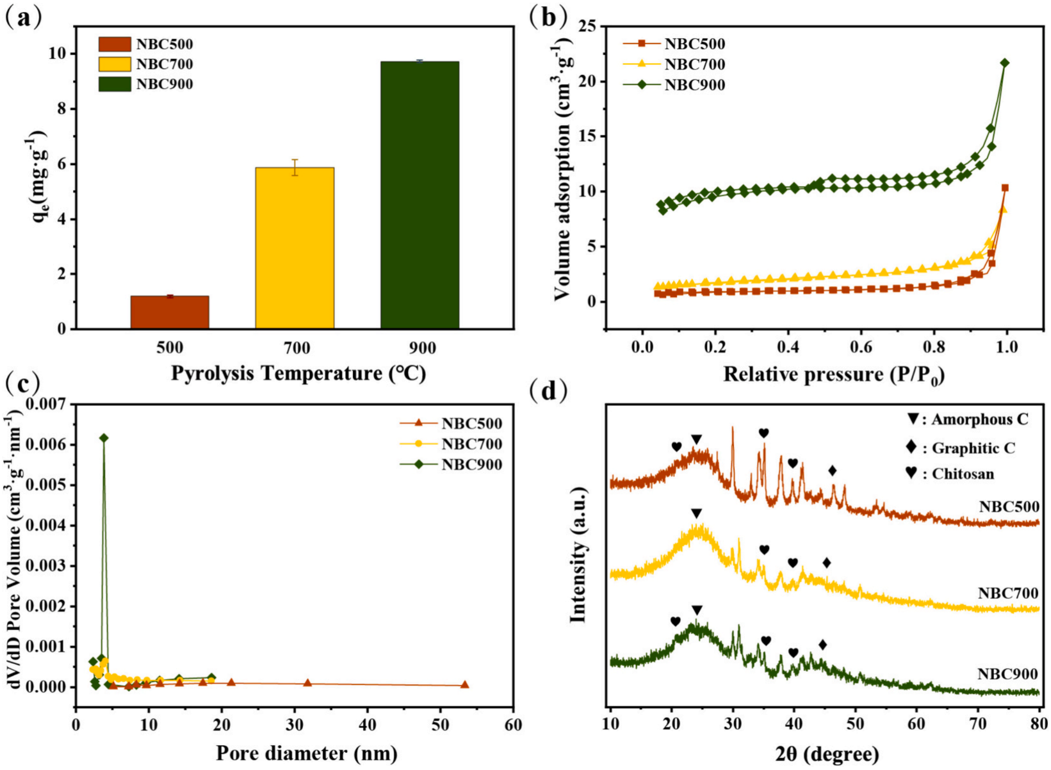

Fig. 1. Characterization of NBC-X: (a) IMI removal efficiency, (b) N_2 adsorption-desorption isotherms, (c) pore size distribution, and (d) XRD spectra.

controlled temperatures (25 °C, 35 °C, and 45 °C). After adsorption, the samples were filtered through a 0.45 μm organic membrane, transferred to 10 mL centrifuge tubes, and stored at 4 °C for subsequent analysis. The IMI concentrations was determined using ultraviolet spectrophotometry (UV-6000, Shanghai Metch Instruments Co., Ltd., China) at a wavelength of 270 nm.

To assess the influence of water chemistry on IMI adsorption, batch experiments were conducted under varying pH conditions, ion types, and humic acid concentrations. Additionally, the adsorption performance of the adsorbent was evaluated in two real water samples to simulate IMI-contaminated environments. The reusability of the adsorbent was investigated through pyrolysis regeneration. Further details on experimental parameters are provided in **Text S4**.

3. Results and discussions

3.1. Adsorption performance comparison among different materials

Fig. 1(a) illustrates the adsorption properties of three NBCs, demonstrating that their equilibrium adsorption capacity for IMI increases with higher pyrolysis temperatures. Notably, NBC900 exhibits superior adsorption performance, achieving an adsorption capacity of 9.723 mg·g^{-1} and a remarkable removal rate of 97.2 % for 10 mg·L^{-1} IMI within 24 h. This performance significantly surpasses that of NBC500 (adsorption capacity: 1.193 mg·g^{-1}, removal rate: 11.9 %) and NBC700 (adsorption capacity: 5.875 mg·g^{-1}, removal rate: 58.8 %). The enhanced adsorption capacity is hypothesized to result from the effect of pyrolysis temperature on the morphology of chitosan on the biochar surface, which may facilitate the development of favorable pore structures and surface functional groups that enhance IMI adsorption [28]. This hypothesis is further explored in the subsequent characterization section.

3.2. Characterizations

3.2.1. Surface morphology and pore structure

The SEM images of NBC500, NBC700, and NBC900 are presented in Fig. 2. As the pyrolysis temperature increases, the framework structure undergoes more severe damage, resulting in a fragmented particle morphology on the adsorbent surface. This observation suggests that secondary pyrolysis enhances the complete decomposition of the original fiber components [29]. The presence of a network-like cracked structure on the adsorbent surface after chitosan loading may be attributed to residual colloids and pyrolysis products formed through crosslinking with chitosan [30,31]. EDS analysis reveals that C remains as the primary element distributed on the adsorbent surface, indicating that the biochar carbon skeleton provides a robust support for chitosan loading. The uniform distribution of N further confirms the homogeneous loading of chitosan colloids onto the adsorbent. Oxygen (O) is mainly concentrated within the network-like cracked structures, demonstrating that addition of chitosan introduces O-containing functional groups, which enhance the adsorption capacity for IMI on the adsorbent surface [31,32].

The bulk elemental composition and ash content of NBC-X are summarized in Table 1. Following chitosan modification, the proportion of C element gradually increases with higher pyrolysis temperatures, while the proportions of N, H, and O decrease. This trend leads to a reduction in the atomic molar ratio of H/C (from 0.017 to 0.014) and (O + N)/C (from 0.432 to 0.139), indicating that higher pyrolysis temperatures enhance the aromaticity of biochar while reducing its hydrophilicity and polarity [6,14,33]. These results suggest that dehydrogenation and deoxidation reactions occur during high-temperature pyrolysis.

Compared to WBC, the chitosan-modified biochars exhibit higher contents of N and O elements (**Table S1**), confirming the introduction of N-containing and O-containing functional groups by chitosan [30,31]. The modification also alters the atomic molar ratio of H/C and (O + N)/C. Specifically, NBC900 shows a higher H/C ratio (0.014) compared to

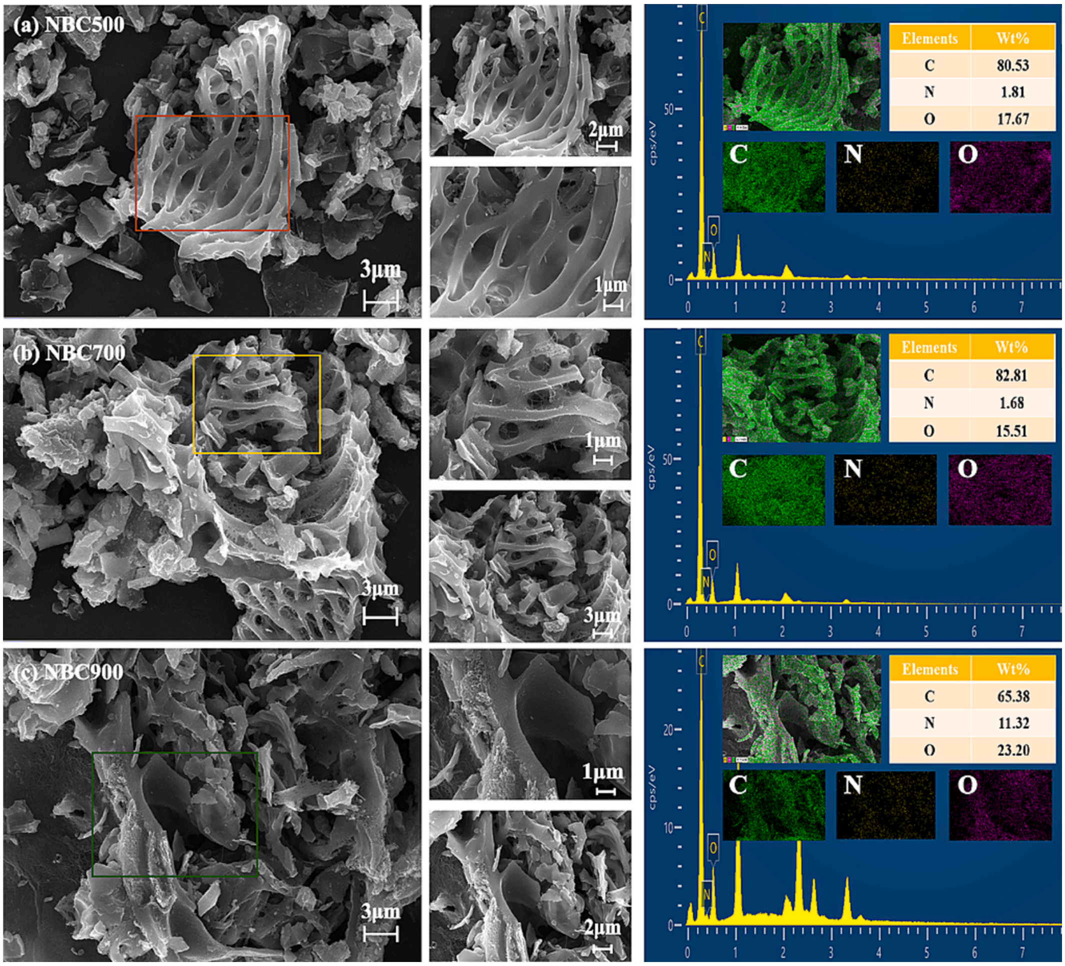

Fig. 2. Morphological and elemental characterization of NBC-X: (a) NBC500, (b) NBC700, and (c) NBC900 showing SEM images with corresponding EDS elemental mappings.

Table 1
Element and ash content.

Biochar	Bulk elemental composition (%)				Ash content (%)	Atomic ratio	
	C	H	N	O		H/C	(O + N)/C
NBC500	62.01	1.056	4.05	22.754	10.1	0.017	0.432
NBC700	65.05	1.018	4.93	18.432	10.6	0.016	0.359
NBC900	75.01	1.025	3.96	6.485	13.5	0.014	0.139

Table 2
Specific surface area and pore parameters of NBC-X.

Biochar	BET ($m^2 \cdot g^{-1}$)	V_{total} ($cm^3 \cdot g^{-1}$)	V_{micro} ($cm^3 \cdot g^{-1}$)	V_{micro}/ V_{total} (%)	Average pore size (nm)
NBC500	3.159	0.0007	0.1645	0.1645	5.3114
NBC700	6.394	0.0072	0.0012	0.1703	4.5898
NBC900	32.918	0.0207	0.0147	0.7125	2.5146

WBC (0.012), while its (O + N)/C ratio (0.139) is lower than that of WBC (0.223). This indicates an increase in aromaticity, hydrophilicity, and polarity after modification [14,29,34]. As the pyrolysis temperature increases from 500 °C to 900 °C, biomass pyrolysis becomes more efficient, with minimal evaporation of inorganic elements. As a result, the ash content of NBC900 rises to 13.5 %, surpassing that of WBC (10.2 %). This suggests the successful incorporation of inorganic substances from chitosan onto the surface of the adsorbent.

The N_2 adsorption-desorption isotherms of NBC-X are presented in Fig. 1(b). The non-overlapping adsorption and desorption isotherms, along with the presence of Type IV isotherms featuring H_3-type hysteresis loops, indicate that the three biochars possess irregular pore sizes and can be classified as mesoporous materials [35]. Additionally, the results depicted in Fig. 1(c) demonstrate that the pore diameter of these biochars ranges from 2 to 5 nm, which aligns with the average pore size values provided in Table 2 and falls within the range associated with mesoporous materials. This finding further confirms that mesoporous constitute the primary structural feature of these three adsorbents [27]. Furthermore, based on data from Table 2, it is evident that chitosan-modified adsorbent materials exhibit an increasing specific surface area with rising pyrolysis temperatures. Specifically, NBC900 possesses a specific surface area of 32.918 $m^2 \cdot g^{-1}$, which is more than ten times greater than that of NBC500 (3.159 $m^2 \cdot g^{-1}$). This indicates a more complete pyrolysis process for chitosan at higher temperatures. Moreover, both the micropore volume and the ratio of micropore volume to total pore volume gradually increase across this series of adsorbent materials, suggesting enhanced availability of IMI adsorption sites for NBC900 and, consequently, improved overall adsorption capacity. This observation is consistent with the superior performance of NBC900 mentioned earlier. In comparison to WBC (**Table S2**), chitosan-modified biochar exhibits a significant decrease in specific surface area. This reduction can be attributed to the obstruction of some pores caused by chitosan loading, resulting in a decrease in total pore volume from 0.056 $cm^3 \cdot g^{-1}$ to 0.0207 $cm^3 \cdot g^{-1}$. Additionally, the secondary pyrolysis

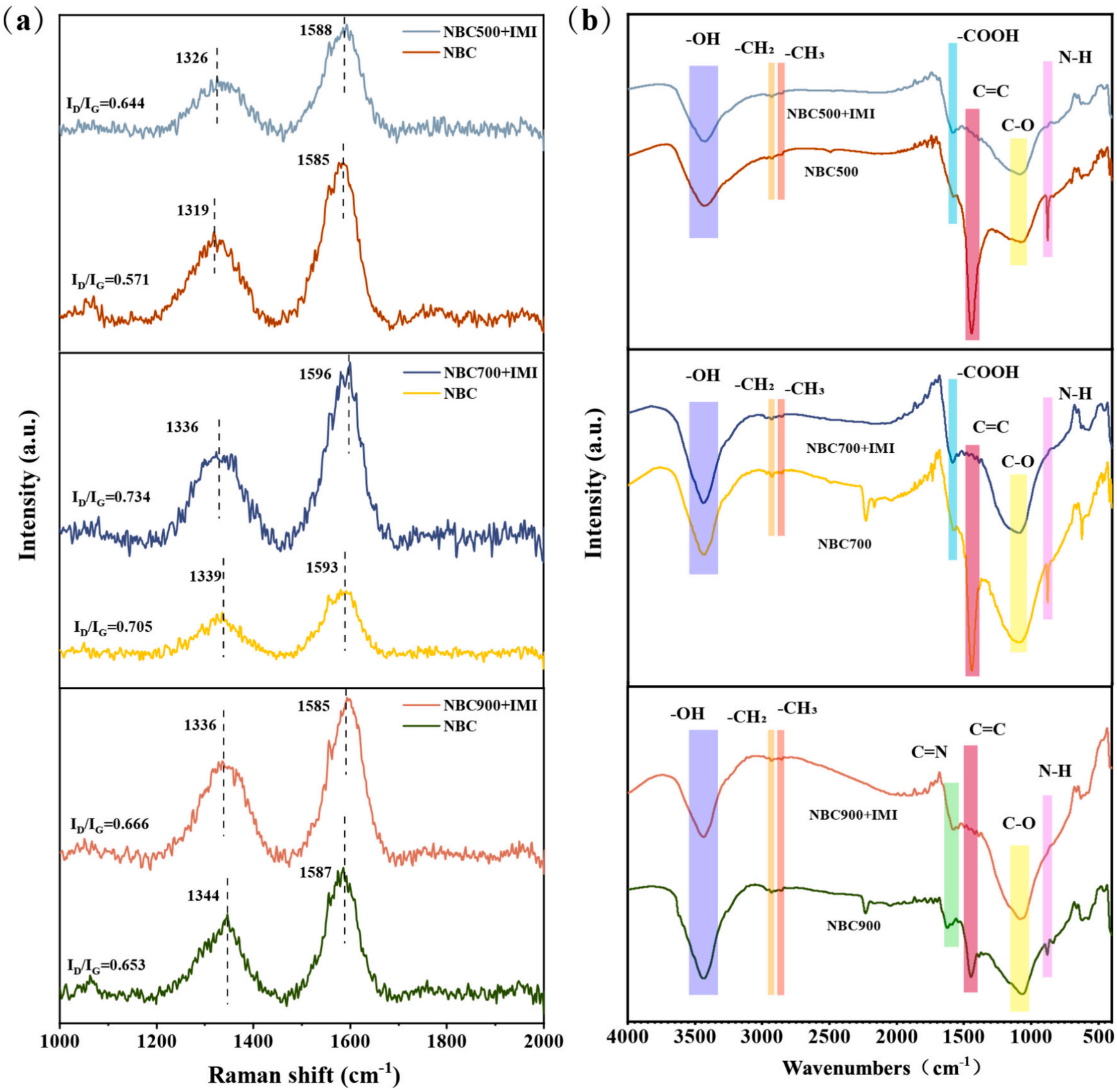

Fig. 3. Comparative spectroscopic analysis of NBC-X: (a) Raman spectra and (b) FT-IR spectra before and after IMI adsorption.

and crushing processes during biochar modification contribute to more extensive pyrolysis of biochar, intensifying the production of fragmented particles and disrupting mesoporous structures.

3.2.2. *Graphitization and defect degrees*

The XRD characterization results of NBC500, NBC700, and NBC900 are presented in Fig. 1(d). The observed diffraction peaks at approximately $2\theta = 22^\circ$ and 44° correspond to the amorphous carbon (002) and slight graphite carbon (111) structures, respectively [36,37]. Additionally, the diffraction peaks near $2\theta = 22^\circ$ and 40.5° represent the characteristic crystal planes of chitosan: (101) and (002), respectively, as reported by Abou El-Reash et al. [38] and He et al. [31]. Notably, the positions and intensities of these peaks vary with pyrolysis temperature, indicating an influence on the crystallization degree of chitosan carbonization products and validating the effectiveness of the modification method employed. The Raman spectra of NBC-X are shown in Fig. 3(a), revealing two prominent characteristic peaks: the D band at approximately 1350 cm^{-1} [39] and the G band near 1590 cm^{-1} [40]. The intensity ratio of the ID/IG serves as an indicator for quantifying the extent of carbon defects in NBC-X [41]. It is evident that as the pyrolysis temperature increases, the ID/IG value of biochar gradually rises, indicating a proportional relationship between pyrolysis temperature and carbon defect degree [37]. Compared to the ID/IG value of 0.919 for WBC (**Fig. S1**), the modified NBC-X exhibits reduced values ranging from 0.571 to 0.653. This reduction can be attributed to the comparable atomic sizes of N and C atoms, enabling their embedding into the C lattice during pyrolysis, thereby reducing disorder and defect levels within the adsorbent structure [42]. Chitosan modification enhances the graphitization degree of biochar, facilitating improved adsorption capacity for IMI through π-π interactions [42,43].

3.2.3. *Surface functional groups*

The FT-IR spectra of NBC-X are shown in Fig. 3(b), illustrating distinct absorption bands at specific wavelengths. The prominent absorption band observed at 3439 cm^{-1} corresponds to the -OH stretching vibration [44]. Additionally, two absorption bands are evident at 2920 cm^{-1} and 2848 cm^{-1}, which can be attributed to the stretching vibrations of aliphatic functional groups (-CH_2 and -CH_3, respectively) [45]. Furthermore, the C=C stretching vibration within the aromatic ring is observed at 1447 cm^{-1} [33]. Notably, an increase in pyrolysis temperature leads to a gradual decrease in the intensity of diffraction peaks for each functional group. This phenomenon arises due to enhanced biomass pyrolysis under high-temperature conditions, resulting in deoxidation and dehydrogenation processes. Simultaneously, the degree of aromatization of biochar materials increases with pyrolysis temperature, leading to higher C content in the carbonized material [13,14].

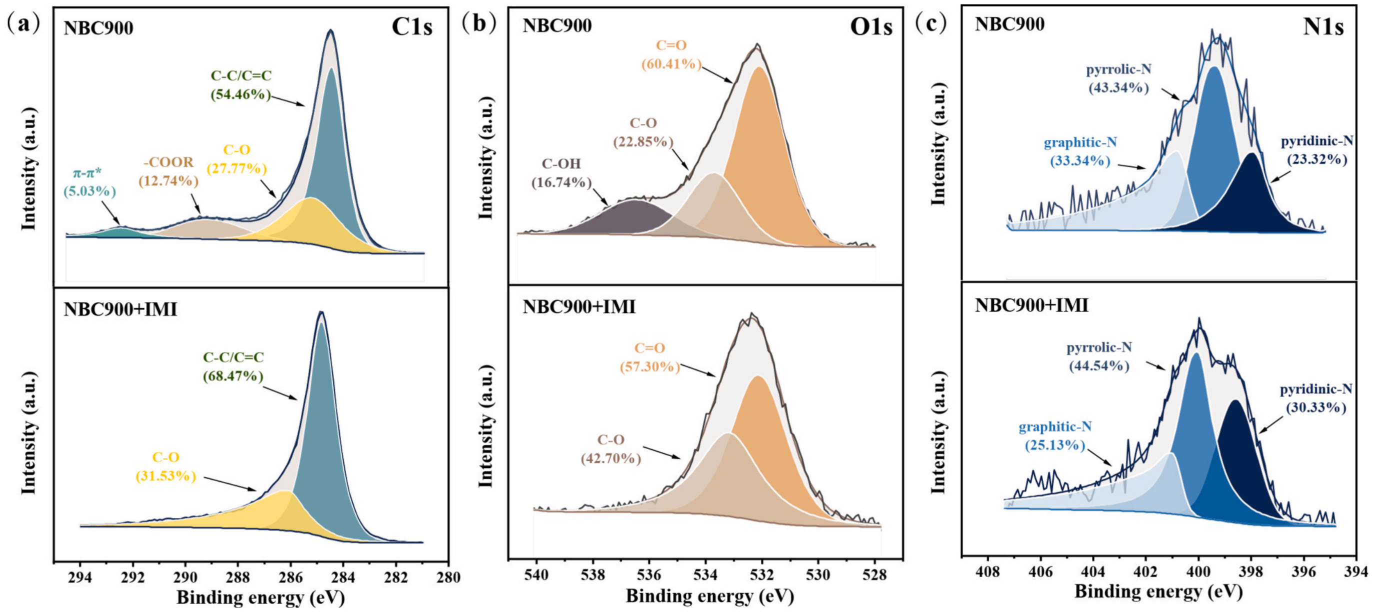

Fig. 4. High-resolution XPS spectra of NBC900: (a) C 1 s, (b) O 1 s, and (c) N 1 s regions before and after IMI adsorption.

The FT-IR characterization results of NBC500 and NBC700 reveal the presence of -COOH functional group stretching at 1633 cm^{-1} [46,47], indicating that chitosan modification enhances the abundance of O-containing functional groups on the biochar surface. Conversely, no corresponding diffraction peaks are observed in NBC900, suggesting a more pronounced decarboxylation of the adsorbent at higher pyrolysis

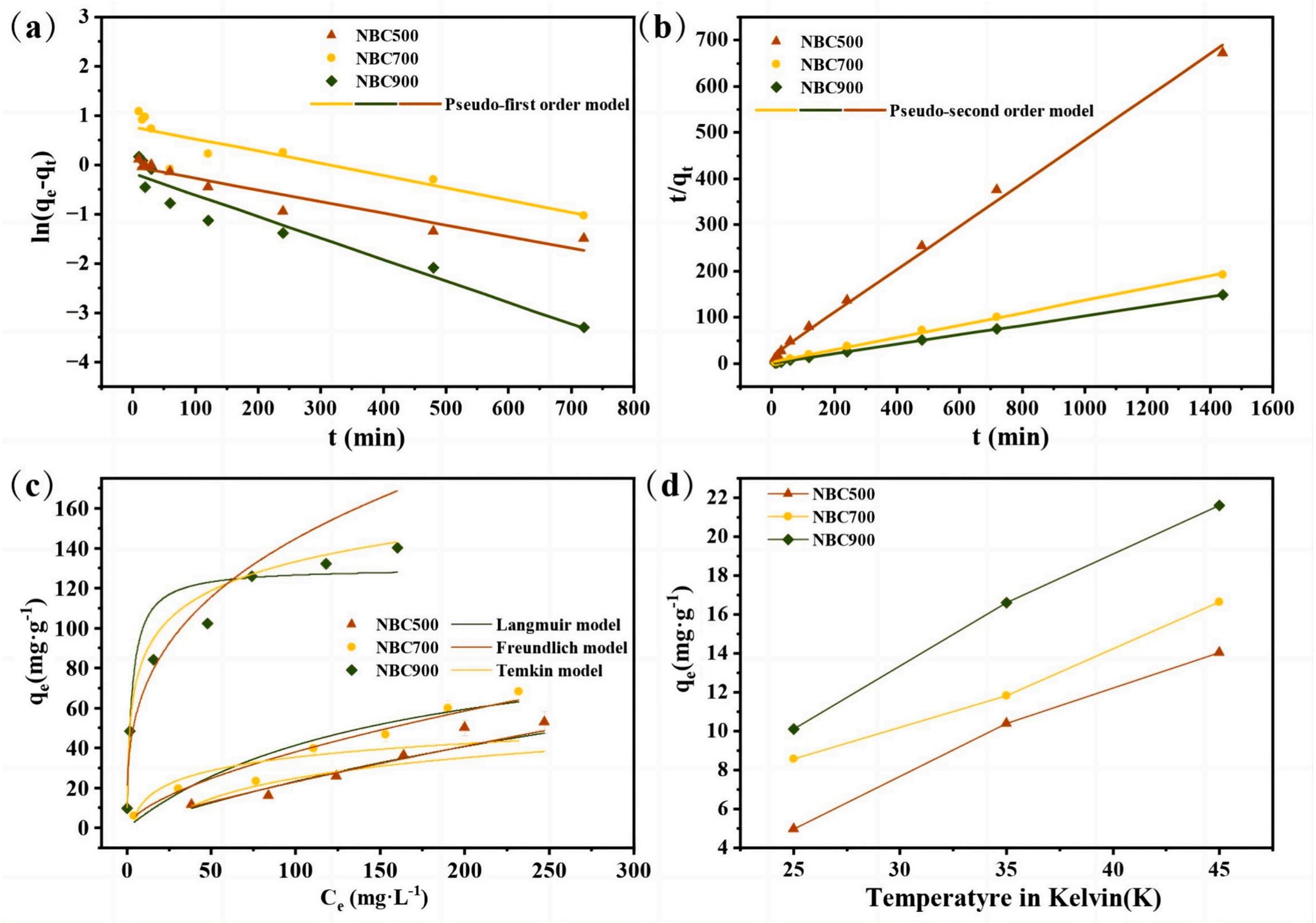

Fig. 5. Adsorption behavior of IMI on NBC-X: (a, b) kinetics profiles, (c) isotherms fitting, and (d) thermodynamic analysis.

temperatures, resulting in the decomposition of -COOH groups [48]. The C—O functional group at 1061 cm^{-1} [49,50] and the C═N functional group at 1653 cm^{-1} [32,51], representing characteristic diffraction peaks of chitosan carbonization products, are attributed to the cross-linking effect of chitosan. Additionally, N—H stretching vibrations at 879 cm^{-1} are detected in NBC900 [13,52], which may arise from the carbonization of chitosan colloids under higher pyrolysis temperatures [53].

To further analyze the surface functional groups, XPS analysis was employed. As shown in Fig. 4(a), high-resolution C1s spectrum of NBC900 exhibits four peaks, corresponding to C-C/C=C (284.8 eV), C—O (286.9 eV), -COOR (290.2 eV), and π-π* (293.3 eV) transition characteristic peaks, as reported by Ding et al. [54] and Cheng et al. [13]. The XPS spectra of NBC500 and NBC700 are presented in **Fig. S2**. In Fig. 4(b), the O1s spectrum displays three characteristic peaks: C═O (532.1 eV), C—O (533.7 eV), and C-OH (536.5 eV). With increasing pyrolysis temperature, the relative proportions of these characteristic peaks change, showing a decreasing trend for -COOR and C—O peaks in the C1s spectrum, as well as a gradual decrease in the total proportion of the C═O and C—O peaks in the O1s spectrum. This indicates that higher pyrolysis temperature result in the decomposition of certain surface groups on biochar, consistent with FT-IR characterization results. Meanwhile, the proportion of C-C/C=C peaks in the C1s spectrum exhibits a gradual decline, indicating a decrease in graphitization degree, which aligns with the conclusion that carbon defects are directly proportional to pyrolysis temperature, as observed from the Raman characterization results. Interestingly, despite the reduced graphitic order, the relative intensity of the π-π* transition peak increases with rising pyrolysis temperature, with NBC900 exhibiting the most pronounced feature. This indicates an enhanced π-electron accepting capacity of the adsorbent, which may result from the generation of defect sites, edge-localized aromatic domains, or small conjugated structures at elevated temperatures [55,56].

In Fig. 4(c), the N1s spectra of NBC900 display three distinct peaks corresponding to pyridine-N (398.1 eV), pyrrole-N (400.1 eV), and graphite-N (401.2 eV), respectively. Compared to NBC500 and NBC700 (**Fig. S2**), the relative content of pyridine-N decreases from 51.7 % to 23.3 %, while the relative content of pyrrole-N and graphite-N increases from 26.4 % and 21.9 % to 43.3 % and 33.3 %, respectively. This can be attributed to the thermal conversion process, where pyrrole-N and pyridine-N transform into graphite-N with increasing pyrolysis temperature [57].

The physical and chemical properties of WBC were significantly altered by chitosan carbonization modification, as demonstrated by the NBC series. This modification led to changes in elemental composition, graphitization degree, and the distribution of surface functional groups. The introduction of N atoms enhanced the hydrophilicity and polarity of biochar materials, resulting in a rearrangement of carbon atoms and an improvement in the degree of graphitization [14,42]. Consequently, more effective adsorption sites for IMI were provided.

3.3. *Adsorption kinetics*

The linear kinetic data fitting curves of NBC500, NBC700, and NBC900 for IMI adsorption are presented in **Fig. 5(a)** and **(b)**, while the corresponding fitting parameters provided in **Table S3**. The pseudo-second-order kinetics model provided a better fit to the adsorption data at each time point, with linear correlation coefficients (R^2) of 0.9961 (NBC500), 0.9982 (NBC700), and 0.9999 (NBC900). Notably, the calculated adsorption capacity (q_e) closely matched the experimental value (q_e'), indicating that the primary mechanism for IMI adsorption by NBC500, NBC700, and NBC900 involves chemical processes, such as electron exchange leading to covalent bond formation or the generation of new compounds [13]. Furthermore, the initial adsorption rate (h, $mg \cdot g^{-1} \cdot min^{-1}$) was determined using the formula $h = K_2^2 q_e^2$ (K_2 represents the rate constant of the pseudo-second-order kinetic model, as detailed in **Text S3**) [58]. Comparing NBC500 and NBC700, which exhibited h values of 0.0601 and 0.3771, respectively, NBC900 demonstrated a significantly higher h value of 2.9264. This observation suggests that the enhanced properties resulting from increased pyrolysis temperature facilitate IMI overcoming mass transfer resistance on the adsorbent surface, thereby improving its overall adsorption performance [3,51].

Table 3
The adsorption isotherm model parameters of NBC-X.

Isotherms models	Parameters	NBC500	NBC700	NBC900
	q_m ($mg \cdot g^{-1}$)	160.9573	104.9287	130.2023
Langmuir	K_L ($L \cdot g^{-1}$)	0.0017	0.0065	0.3491
	R^2	0.9224	0.8872	0.9921
	1/n	0.8254	0.6199	0.3247
Freundlich	K_F ($mg^{(1\text{-}n)}$ $L \cdot g^{-1}$)	0.5156	2.1914	32.4611
	R^2	0.9406	0.9551	0.8389
	K_e ($L \cdot mg^{-1}$)	0.0539	0.3834	5.8849
Temkin	b_T	153.7707	233.6489	108.5991
	R^2	0.8458	0.7499	0.9978

To further investigate the adsorption process and identify the main rate-limiting steps, the intraparticle diffusion model was employed. **Fig. S3** illustrates the fitting results of the intraparticle diffusion model for NBC500, NBC700, and NBC900, while **Table S4** presents the corresponding fitting parameters. The adsorption process can be divided into three stages: **Stage I**: this stage corresponds to liquid film diffusion. Characterized by a steep slope, indicating higher adsorption efficiency due to the abundance of available adsorption sites on the adsorbent surface. During this stage, IMI diffuses directly from solution to the adsorbent surface. **Stage II**: this stage represents intraparticle diffusion. The K_{II} values for NBC900 and NBC700 are significantly lower than K_{I}, suggesting that intraparticle diffusion is the primary rate-limiting step for IMI adsorption by these two adsorbents [51,59]. In contrast, although NBC500 exhibits a greater K_{II} value compared to K_{I}, both its K_{I} and K_{II} values are small, indicating a low intrinsic IMI adsorption rate. Therefore, for NBC500, liquid film diffusion is considered the main rate-limiting step throughout the entire adsorption process. The liquid film diffusion process is closely associated with the pore structure of the adsorbent, and the low specific surface area of NBC500 plays a crucial role in limiting the adsorption rate of IMI. **Stage III**: this stage represents the distribution effect, where IMI is adsorbed through physical and chemical processes. This stage involves a dynamic equilibrium between IMI in solution and on the adsorbent surface, which is typically not considered a rate-limiting step.

The thickness of the boundary layer can be quantified by the C value (**Table S4)**. The C_{II} values for all three adsorbents during IMI adsorption are higher than C_{I}, indicating that intraparticle diffusion serves as the primary rate-limiting step [51,60]. In simpler terms, IMI undergoes transfer from the liquid solution to the adsorbent surface, traverses internal pores within the adsorbent, and reaches equilibrium when the rates of adsorption and desorption are equal. The process is controlled by two key mechanisms: liquid film diffusion and intraparticle diffusion. Notably, intraparticle diffusion is particularly significant due to NBC500's inherently low affinity for IMI. Thus, both liquid film diffusion and intraparticle diffusion act as main rate-limiting steps during NBC500-mediated IMI adsorption.

3.4. *Adsorption isotherms*

The relationship between adsorption equilibrium and adsorption capacity of NBC-X is illustrated in Fig. 5(c). The theoretical maximum adsorption capacities for IMI by NBC500, NBC700, and NBC900 were determined to 52.9 $mg \cdot g^{-1}$, 68.2 $mg \cdot g^{-1}$, and 140.1 $mg \cdot g^{-1}$, respectively. The Langmuir and Freundlich isotherm models are widely employed to characterize the adsorption behavior of adsorbents. Table 3

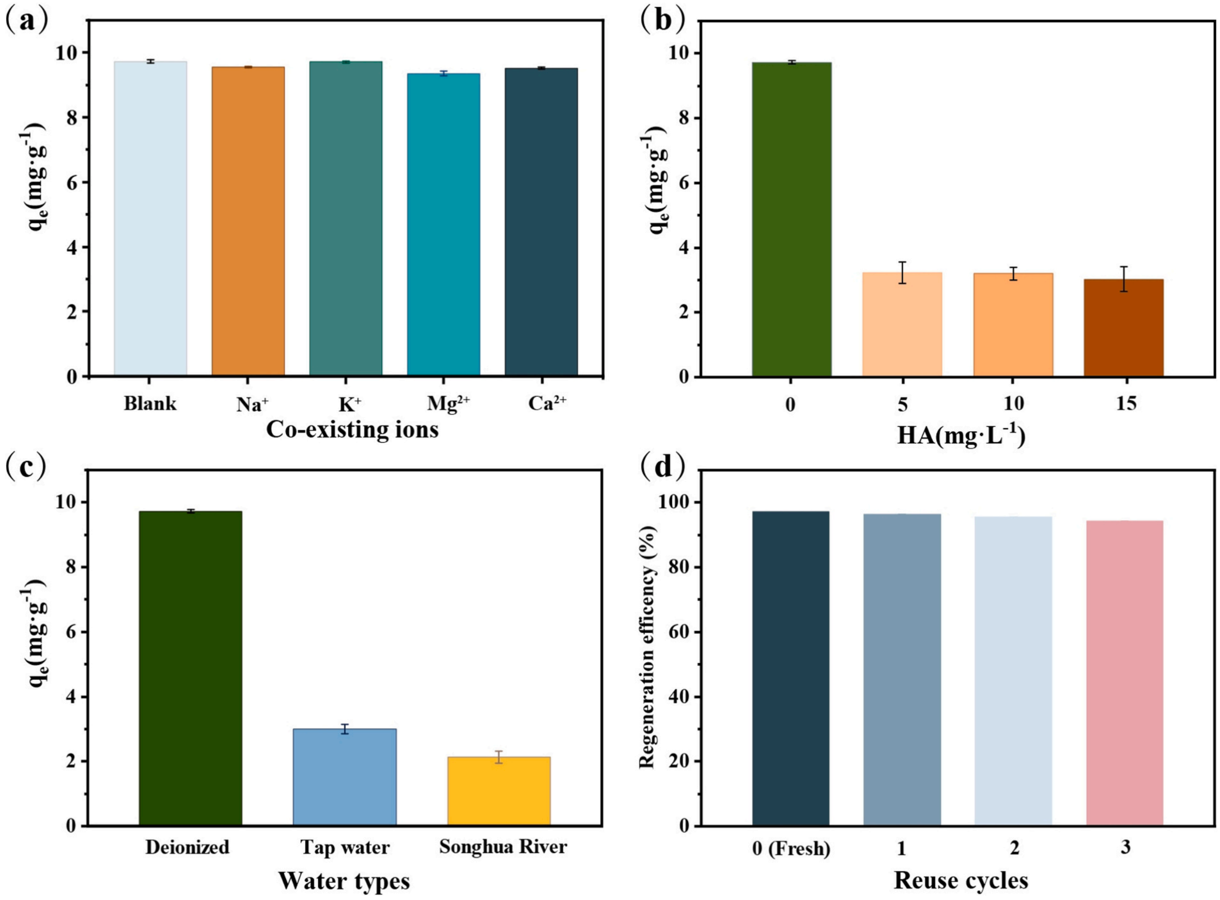

Fig. 6. Adsorption performance of NBC900 under different conditions: (a) co-existing ions, (b) HA concentration, (c) real water matrices, and (d) regeneration cycles.

summarizes the parameters of the isotherm models used for fitting, revealing distinct variations in model performance among the three adsorbents. Notably, the analysis of IMI adsorption by NBC900 revealed that the Langmuir isotherm model ($R^2 = 0.9921$) exhibited a higher correlation coefficient compared to the Freundlich isotherm model ($R^2 = 0.8389$), indicating the adsorption behavior observed in this study is more accurately described by the Langmuir isotherm model. Furthermore, with a predicted value (130.2 mg·g^{-1}) closer to the experimental measured value (140.1 mg·g^{-1}), it can be inferred that NBC900 possesses a uniform distribution of adsorption sites, suggesting monolayer adsorption behavior where the adsorbate uniformly covers the adsorbent surface [61]. In contrast, the adsorption process of IMI by NBC700 and NBC500 were more consistent with the Freundlich isotherm model, as evidenced by correlation coefficients of $R^2 = 0.9551$ and 0.9406, respectively. This implies heterogeneous adsorption for these two adsorbents, where the adsorbent surface comprises various adsorption sites, and the adsorption process is conceptualized as a multi-layer phenomenon involving interactions between adsorbate molecules [26]. For the Lamgmuir isotherm model fitting parameters of NBC900, the constant $K_L = 0.3491$, which falls within the range of 0 and 1, indicating favorable conditions for IMI adsorption [6,61]. In the Freundlich isotherm model, the value of 1/n serves as an indicator of the adsorption difficulty between the adsorbate and adsorbent. Specifically, when $1/n < 1$, the adsorption process occurs easily; otherwise, it is more challenging. For NBC700 and NBC500, the values for 1/n were determined to be 0.6199 and 0.8254, respectively, signifying that both adsorbents exhibit an affinity for IMI. Additionally, with increasing surface coverage, the bond energy distribution becomes more uniform, accompanied by a linear decrease [24]. The Temkin model demonstrates a linear reduction in adsorption energy with increasing surface coverage, elucidating the chemical interplay between the adsorbate and adsorbent [62]. The adsorption of IMI by NBC900 exhibits a higher linear correlation coefficient ($R^2 = 0.9978$), indicating the predominant role of chemical adsorption in the process. Conversely, for NBC500 and NBC700, the smaller nonlinear correlation coefficients suggest that chemical interactions are not the sole driving force for IMI adsorption. The variation in fitting results among the three adsorbents can be attributed to the different degrees of chitosan colloid pyrolysis at varying temperatures. At 500 °C and 700 °C, incomplete pyrolysis leads to residual colloidal particles, aligning more closely with the Freundlich isotherm model. In contrast, at 900 °C, complete pyrolysis eliminates these particles and forms a network-like cracked film structure with evenly distributed adsorption sites, facilitating uniform monolayer adsorption of IMI. In this case, the Lamgmuir isotherm model provides a better description of the overall adsorption process.

In **Table S5**, a comparison was made between the maximum saturated adsorption capacities of the three adsorbents in this study and those of existing chitosan-biochar hydrogel beads and some N-doped biochar adsorbents for organic pollutant adsorption in water. The results revealed that NBC900 exhibited superior adsorption performance compared to most other materials, highlighting the potential application of chitosan-modified white melon seed shell biochar in IMI pollution remediation in the environment.

3.5. *Thermodynamic analysis*

Thermodynamic parameters serve as crucial indicators for elucidating the adsorption mechanism of adsorbents. As depicted in Fig. 5(d), the equilibrium adsorption capacity of NBC-X gradually increases with rising ambient temperature when the initial concentration of IMI is set at

30 mg·L^{-1}. The corresponding thermodynamic parameters are presented in **Table S6**. Throughout the adsorption process of IMI on all three adsorbents, ΔH consistently remains positive, indicating endothermic behavior and suggesting that higher temperatures enhance the adsorption capacity of the adsorbent for IMI [63,64]. A ΔH value below 40 kJ·mol^{-1} is considered indicative of physical adsorption as the primary mechanism [64]. Specifically, as pyrolysis temperature increases, the ΔH values for NBC500, NBC700, and NBC900 rise to 28.135 kJ·mol^{-1}, 51.492 kJ·mol^{-1}, and 60.414 kJ·mol^{-1}, respectively, indicating a progressive contribution from chemical adsorption [10]. The thermodynamic parameters reveal that $\Delta G < 0$ denotes a spontaneous process for IMI adsorption by NBC500, NBC700, and NBC900. Moreover, the absolute value of ΔG increases with temperature, substantiating enhanced spontaneity of adsorption at elevated ambient temperatures [65]. Notably, among the materials studied, NBC900 exhibits the highest absolute value of ΔG, which directly correlates with its superior adsorption capacity. Furthermore, a positive $\Delta S > 0$ signifies strong affinity between IMI and the adsorbent, suggesting an entropy-driven process accompanied by increased ion disorder at the solid/liquid interface [66]. Therefore, the adsorption of IMI by NBC-X can be characterized as an endothermic, spontaneous, and disordered process, exhibiting significant interaction with IMI.

3.6. *Effect of pH, ionic types, and humic acid*

Given the high-efficiency adsorption performance of NBC900, we investigated the influence of various water chemistry factors on its adsorption capacity for IMI. The solution pH plays a crucial role in controlling the adsorption behavior of NBC900 by affecting both the molecular morphology of pollutants and the surface charge of the adsorbent [7]. Since IMI is an amphoteric molecule, it exhibits pKa values of 1.56 and 11.12, respectively. This implies that at pH > 11.12, the surface of IMI molecules predominantly carries negative charges, while at 1.56 < pH < 11.12, they exist mainly in an ionized form (IMI±) [24]. As depicted in **Fig. S3(a)**, there is no significant change in the adsorption capacity of NBC900 for IMI within a pH range of 2 to 11. Considering its pH_{PZC} value of 11.3, as shown in **Fig. S3(b)**, it can be inferred that NBC900 predominantly carries positive charges within the pH range of 2 to 11. Consequently, under these conditions, IMI molecules exist in a neutral ionized state. Therefore, electrostatic adsorption resulting from surface charge is not considered the primary mechanism for adsorption [3].

The presence of metal ions in natural water can influence the adsorption performance of the adsorbent by competing with IMI for available adsorption sites [42]. To investigate its practical application in terms of adsorption capacity, background solutions containing Na^+, K^+, Ca^{2+}, and Mg^{2+} at a concentration of 0.5 mol·L^{-1} were prepared and diluted with IMI mother liquor. Fig. 6(a) illustrates that the equilibrium adsorption capacity of NBC900 for IMI varies when exposes to different metal ions. In the case of K^+, there is a slight improvement in NBC900's adsorption capacity for IMI, possibly attributed to an increase in ionic strength, leading to enhanced activity coefficients and reduced solubility, thereby promoting adsorption [67]. Conversely, the presence of Na^+ has minimal impact on the overall adsorption performance, suggesting weak salting-out enhancement effects induced by ionic compounds or potential offsetting between these effects and agglomeration inhibition caused by the adsorbents [49,65,68]. However, the participation of Ca^{2+} and Mg^{2+} in adsorption significantly decreases the adsorption capacity of the adsorbent. This decrease may be attributed to the formation of IMI-Ca/Mg complexes between Ca^{2+} and Mg^{2+}, as reported by Feng et al. [50], which reduces the affinity of IMI toward the adsorbent. Additionally, Ca^{2+} and Mg^{2+} react with the O-containing functional groups on the surface of the adsorbent, as indicated by Ke et al. [35] and Ma et al. [43], leading to the occupation of more active sites and inhibition of IMI adsorption by NBC900. Moreover, in an ionic environment constructed by divalent ions (Ca^{2+} and Mg^{2+}), the concentration of Cl^- is twofold that of monovalent ions (Na^+ and K^+). Consequently, Cl^- may exhibit enhanced affinity toward the adsorbent surface, thereby occupying active sites and subsequently diminishing the adsorption capacity. In summary, when various metal ions are present, NBC900 exhibits a 3.9 % reduction in its adsorption capacity, demonstrating significant tolerance toward interference from ionic strength—an indication of its excellent anti-interference ability.

Humic acid (HA), composed of aromatic rings and fatty acids with abundant hydroxyl and π electrons, was selected to investigate its impact on the adsorption of NBC900 for IMI [69]. As shown in Fig. 6(b), the adsorption capacity of NBC900 for IMI exhibited a significant decrease with increasing HA concentration, declining from 9.723 mg·g^{-1} to 3.028 mg·g^{-1}. The competitive adsorption between IMI and HA on NBC900 is attributed to hydrogen bonding, electrostatic interactions, π-π interactions, as well as complexation or the formation of HA-IMI compounds, which diminish the affinity toward IMI [70]. Furthermore, the larger molecules of HA occupy certain adsorption sites on NBC900, resulting in pore blockage [71].

3.7. *The adsorption performance of NBC for IMI in various real waters*

To further validate the adsorption performance of NBC for IMI, various real water samples, including deionized water, tap water, and river water, were utilized. The basic physicochemical properties of these water samples are detailed in **Table S7**. Tap water was sourced from Northeast Agricultural University, while the river water was collected from the Harbin section of the Songhua River (45°46′ N, 126°36′ E). As illustrated in Fig. 6(c), NBC900 exhibited significant IMI adsorption capacities in deionized water (9.723 mg·g^{-1}), tap water (2.999 mg·g^{-1}), and river water (2.132 mg·g^{-1}). The observed decline in adsorption capacity across these water types aligns with the influence of HA on adsorption behavior. Consequently, it can be inferred that the competitive adsorption of HA with IMI significantly reduces the adsorption performance of NBC900 for IMI. This reduction is likely due to HA occupying specific adsorption sites or causing pore blockage [26,43].

3.8. *Reusability of NBC900*

Regeneration capacity is a critical parameter for evaluating the long-term applicability of adsorbents in organic pollutant remediation. While conventional regeneration methods typically employ organic solvent extraction and washing techniques [72], these approaches often introduce secondary pollution challenges due to the residual pollutants in the solvents. In this study, the adsorbents were synthesized via pyrolysis, thereby inherently exhibiting a high degree of thermal stability. Leveraging this property, we proposed an innovative regeneration strategy based on thermal pyrolysis, enabling the high-temperature decomposition of adsorbed pollutants. As demonstrated in Fig. 6(d), NBC900 maintained excellent adsorption performance after three regeneration cycles, with IMI (10 mg·L^{-1}) removal efficiency decreasing only marginally from 97.2 % to 94.4 %. This minimal performance reduction underscores the exceptional thermal stability of NBC900 and suggests that the re-pyrolysis process mainly eliminates surface-adsorbed IMI. Consequently, it is reasonable to infer that no significant structural alterations occurred during the regeneration process. These results validate the practical applicability of NBC900 and support its potential for sustainable environmental remediation.

3.9. *Adsorption mechanisms*

Comprehensive experimental and characterization data demonstrate that IMI adsorption by NBC900 involves synergistic physisorption and chemisorption. Physisorption, primarily governed by diffusion processes and pore-filling effects, contributes significantly to the rate-limiting steps. The substantial SSA and optimal pore size distribution of NBC900 facilitate effective IMI adsorption by providing abundant

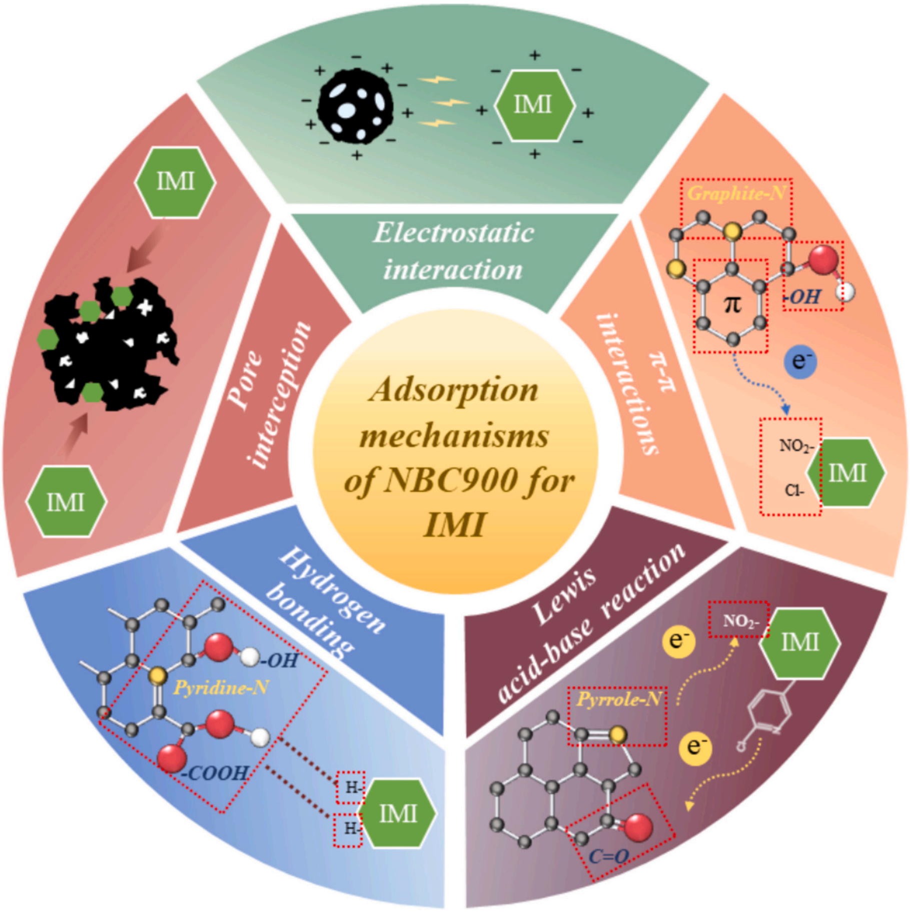

Fig. 7. Proposed adsorption mechanism of IMI on NBC900 in aqueous systems: pore filling, electrostatic interaction, hydrogen bonding, π-π interactions, and Lewis acid-base interactions.

accessible sites. While electrostatic interactions may contribute to adsorption, as suggested by pH-dependent experiments, the minimal ionic strength effect indicates their secondary role. These observations collectively suggest that chemisorption dominates the adsorption process, a characteristic enhanced by NBC900's N-doped structure.

In comparison with previous studies on N-doped biochar adsorbents, our results offer more detailed insights into the specific roles of N functionalities. Cheng et al. [13] synthesized N-doped biochar from cellulose and melamine for atrazine removal, and our study identifies similar adsorption enhancements mediated by N functionalities-particularly pyridinic-N and graphitic-N. However, while their study primarily attributed the improved adsorption to increased specific surface area and π-π interactions, our findings further reveal specific electron transfer mechanisms (e.g., pyridinic-N acting as a Lewis base interacting with the -NO_2 group of IMI), thereby offering a more comprehensive understanding of N-related chemisorption. Similarly, Guy Laurent Zanli et al. [14] investigated norfloxacin adsorption onto urea-modified cocoa shell biochar, highlighting pore filling, hydrogen bonding, and π-π interactions facilitated by graphitic-N and oxidized-N. Our findings support these mechanisms and further clarify the distinct role of pyrrolic-N in enhancing hydrogen bonding through modulation of surface electronegativity, with graphitic-N contributing to π-electron donation.

XRD analysis (Fig. 1(d)) further confirms the presence of well-developed graphite carbon (111) structures in NBC900, indicating advanced carbonization. This graphitic framework enables π-electron donation, while IMI's chlorine (—Cl) and nitro (-NO_2) groups serve as effective π-electron acceptors. Raman spectroscopy (Fig. 3(a)) reveals increased ID/IG ratios post-adsorption, further evidencing the participation of graphitic carbon in IMI adsorption [39,40,73,74]. These findings collectively demonstrate that π-π interactions between NBC900's graphitic structure and IMI's aromatic ring drive chemisorption [75,76].

FT-IR spectral changes (Fig. 3(b)) indicate significant modifications in surface functional groups post-adsorption. The attenuation of C═N and -COOH peaks, along with the disappearance of C═C and N—H vibrations, suggests their involvement in adsorption. Hydrogen bonding likely occurs between IMI's hydrogen atoms and NBC900's -OH, -CH_2, -CH_3, -COOH, and N—H groups [76,77]. Additionally, O-containing moieties and graphitic structures (C═N and C═C) may participate in π-π interactions with IMI's —Cl and-NO_2 groups [33,71].

Fig. 4**(a)** and **(b)** present the high-resolution XPS spectra of C1s and O1s for NBC900 after IMI adsorption. The disappearance of characteristic peaks (e.g., -COOR, π-π*, and C-OH) post-adsorption confirms π-π interactions between NBC900 and IMI. Specifically, the attenuated C═O peak intensity in the O1s spectrum confirms its role as a Lewis acid that participates electron transfer with the pyridine ring (Lewis base) of IMI [77]. Notably, the N 1 s spectral evolution reveals significant changes in pyridine-N, pyrrole-N, and graphite-N contents upon adsorption, directly implicating these functional groups in IMI uptake: (1) Pyridine-N (Lewis base) exhibits reduced content, suggesting electron transfer to IMI's -NO_2 group (Lewis acid), facilitating chemical adsorption via Lewis acid-base reactions [43,71]; (2) Pyrrole-N enhances hydrogen bonding with IMI's H atoms by lowering surface electronegativity [78]; and (3) Graphite-N promotes graphitization, reinforcing π-electron interactions, as corroborated by Raman data [13]. Adsorption kinetics and isotherms align with the pseudo-second-order kinetic model and Langmuir/Temkin models, indicating homogeneous monolayer adsorption dominated by chemisorption [62]. Thermodynamic parameters ($\Delta G < 0$、$\Delta S > 0$ and $\Delta H > 0$) further confirm a spontaneous, endothermic process with increased disorder [66].

The adsorption of IMI onto NBC900 arises from synergistic physical and chemical mechanisms: (1) Physical processes: IMI migrates into NBC900's pores via liquid-film diffusion and intraparticle diffusion, with pore filling further enhancing uptake; and (2) Chemical interactions: Dominant forces include π-π stacking, hydrogen bonding, electrostatic attraction, and Lewis acid-base reactions (e.g., pyridine-N/$-NO_2$ electron transfer). Fig. 7 schematically summarizes these multiscale interactions, highlighting NBC900's efficiency in IMI removal. The combined mechanisms explain the high adsorption capacity and equilibrium kinetics observed experimentally.

4. Conclusions

This study successfully synthesized NBC through a secondary pyrolysis approach using white melon seed shell and chitosan as precursors. The optimized NBC900 exhibited exceptional adsorption capacity for IMI (140.1 $mg \cdot g^{-1}$ at 298 K), attributed to its hierarchical porous structure, high specific surface area, and unique chemical properties, including graphitic carbon domains and N-active sites. Multimodal characterization (XRD, Raman spectroscopy, XPS, and FT-IR) revealed adsorption mechanisms, dominated by π-π interactions and Lewis acid-base reaction, with additional contributions from pore filling, hydrogen bonding, and electrostatic interactions. Notably, the Lewis acid-base interactions between pyridinic-N and carbonyl groups on NBC900 and the nitro group and pyridine ring in IMI were identified as a key mechanistic driver, providing molecular-level insights into the selective adsorption of N-containing pollutants. The practical applicability of NBC900 was further validated through its robust performance in complex environmental matrices, including high efficiency across a wide pH range (2–11), strong resistance to ionic strength variations, and excellent recyclability. The significant impact of humic acid (HA) on adsorption performance in real water systems underscores the predominant role of chemical group interactions compared to adsorption mechanisms.

Beyond its immediate application for IMI removal, this study significantly advances the fundamental understanding of biochar-pollutant interactions, particularly for NNIs and other N-containing contaminants with pyridine ring structures. The innovative synthesis strategy, which streamlines the conventional chitosan-modified biochar preparation by eliminating the need for hydrogel microsphere formation, represents a notable simplification in fabrication processes. These findings not only highlight the potential of NBC900 as a sustainable and efficient adsorbent but also establish a mechanistic framework for designing targeted remediation strategies, contributing to both resource utilization and ecological protection.

CRediT authorship contribution statement

Fuxiang Zhang: Writing – original draft, Visualization, Data curation. **Jialin Lv:** Writing – original draft, Visualization, Methodology, Investigation. **Fengyang Pan:** Visualization. **Qiang Fu:** Methodology, Conceptualization. **Hongliang Jia:** Methodology, Data curation. **Yi-Fan Li:** Methodology, Conceptualization. **Rupert Hough:** Writing – review & editing, Investigation. **Zulin Zhang:** Methodology, Investigation. **Song Cui:** Writing – review & editing, Supervision, Resources, Methodology, Funding acquisition, Conceptualization. **Guorui Liu:** Writing – review & editing, Methodology.

Declaration of competing interest

The authors declare that they have no known competing financial interests or personal relationships that could have appeared to influence the work reported in this paper. Guorui Liu is a member of editoral board of Environmental Chemistry and Ecotoxciology and was not involved in the editorial review or the decision to publish this article.

Acknowledgments

This work was supported by the National Natural Science Foundation of China (No. 52479037), the Distinguished Youth Science Foundation of Heilongjiang Province, China (JQ2023E001), and Young Leading Talents of Northeast Agricultural University, China (NEAU2023QNLJ-013 and NEAU2024QNLJ-01).

Appendix A. Supplementary data

Supplementary data to this article can be found online at https://doi.org/10.1016/j.enceco.2025.07.023.

Data availability

The datasets used or analyzed during the current study are available from the corresponding author on reasonable request.

References

[1] C. Bass, I. Denholm, M.S. Williamson, R. Nauen, The global status of insect resistance to neonicotinoid insecticides, Pestic. Biochem. Physiol. 121 (2015) 78–87.

[2] V.J. Gaffney, C.M.M. Almeida, A. Rodrigues, E. Ferreira, M.J. Benoliel, V. V. Cardoso, Occurrence of pharmaceuticals in a water supply system and related human health risk assessment, Water Res. 72 (2015) 199–208.

[3] D.T. Webb, M.R. Nagorzanski, M.M. Powers, D.M. Cwiertny, M.L. Hladik, G. H. LeFevre, Differences in neonicotinoid and metabolite sorption to activated carbon are driven by alterations to the insecticidal pharmacophore, Environ. Sci. Technol. 54 (22) (2020) 14694–14705.

[4] M.L. Hladik, A.R. Main, D. Goulson, Environmental risks and challenges associated with neonicotinoid insecticides, Environ. Sci. Technol. 52 (2018) 3329–3335.

[5] Z.K. Liu, L.M. Zhang, Z.L. Zhang, L.H. An, R. Hough, P. Hu, Y.-F. Li, F.X. Zhang, S. Wang, Y.Q. Zhao, Y.X. Ke, S. Cui, A review of spatiotemporal patterns of neonicotinoid insecticides in water, sediment, and soil across China, Environ. Sci. Pollut. Res. 29 (37) (2022) 55336–55347.

[6] Y. Chun, G. Sheng, C.T. Chiou, B. Xing, Compositions and sorptive properties of crop residue-derived chars, Environ. Sci. Technol. 38 (2004) 4649.

[7] B.K. Nandi, A. Goswami, M.K. Purkait, Adsorption characteristics of brilliant green dye on kaolin, J. Hazard. Mater. 161 (2009) 387–395.

[8] M.Z. Yameen, S.R. Naqvi, D. Juchelková, M.N.A. Khan, Harnessing the power of functionalized biochar: progress, challenges, and future perspectives in energy, water treatment, and environmental sustainability, Biochar 6 (2024) 25.

[9] M. Larsbo, E. Löfstrand, U.B. DvA de Veer, Pesticide leaching from two Swedish topsoils of contrasting texture amended with biochar, J. Contam. 147 (2013) 73–81.

[10] K.Y. Urbain, E.K. Fodjo, D. Ardjouma, B.Y. Serge, E.S. Aime, G.B.I. Marc, T. Albert, Removal of imidacloprid using activated carbon produced from ricinodendron Heudelotii shells, Bull. Chem. Soc. Ethiop. 31 (2018) 397.

[11] X. Chen, W.-D. OH, Z.-T. Hu, Y.-M. Sun, R.D. Webster, S.-Z. Li, T.-T. Lim, Enhancing sulfacetamide degradation by peroxymonosulfate activation with N-doped graphene produced through delicately-controlled nitrogen functionalization via tweaking thermal annealing processes, Appl. Catal. B Environ. 225 (2018) 243–257.

[12] S.J. Ye, G.M. Zeng, X.F. Tan, H.P. Wu, J. Liang, B. Song, N. Tang, P. Zhang, Y. Y. Yang, Q. Chen, X.P. Li, Nitrogen-doped biochar fiber with graphitization from Boehmeria nivea for promoted peroxymonosulfate activation and non-radical degradation pathways with enhancing electron transfer, Appl. Catal. B Environ. 269 (2020) 118850.

[13] Y.Z. Cheng, B.Y. Wang, J.M. Shen, P.W. Yan, J. Kang, W.Q. Wang, L.B. Bi, X. W. Zhu, Y.B. Li, S.Y. Wang, S.L.L. hen, Z.L. Chen, Preparation of novel N-doped biochar and its high adsorption capacity for atrazine based on π-π electron donor-acceptor interaction, J. Hazard. Mater. 432 (2022) 128757.

[14] B.L. Guy Laurent Zanli, W. Tang, J.W. Chen, N-doped and activated porous biochar derived from cocoa shell for removing norfloxacin from aqueous solution: performance assessment and mechanism insight, Environ. Res. 214 (3) (2022) 113951.

[15] M. Ihara, K. Matsuda, Neonicotinoids: molecular mechanisms of action, insights into resistance and impact on pollinators, Curr. Opin. Insect. Sci. 30 (2018) 86–92.

[16] A. Mandal, N. Singh, T.J. Purakayastha, Characterization of pesticide sorption behavior of slow pyrolysis biochars as low-cost adsorbent for atrazine and imidacloprid removal, Sci. Total Environ. 557 (2017) 376–385.

[17] X.H. Yi, C. Zhang, H.B. Liu, R.R. Wu, D. Tian, J.J. Ruan, T. Zhang, M.Z. Huang, G. G. Ying, Occurrence and distribution of neonicotinoid insecticides in surface water and sediment of the Guangzhou section of the Pearl River, South China, Environ. Pollut. 251 (2019) 892–900.

[18] A.M. Sadaria, S.D. Supowit, R.U. Halden, Mass balance assessment for six neonicotinoid insecticides during conventional wastewater and wetland treatment: nationwide reconnaissance in United States wastewater, Environ. Sci. Technol. 50 (12) (2016) 6199–6206.

[19] Z.K. Liu, S. Cui, L.M. Zhang, Z.L. Zhang, R. Hough, Q. Fu, Y.-F. Li, L.H. An, M. Z. Huang, K.Y. Li, Y.X. Ke, F.X. Zhang, Occurrence, variations, and risk assessment of neonicotinoid insecticides in Harbin section of the Songhua River, Northeast China, Environ. Sci. Ecotechnol. 8 (2021) 100128.

[20] W. Yang, S.L. Carmichael, E.M. Roberts, S.E. Kegley, A.M. Padula, P.B. English, G. M. Shaw, Residential agricultural pesticide exposures and risk of neural tube defects and orofacial clefts among offspring in the San Joaquin Valley of California, Am. J. Epidemiol. 179 (2014) 740–748.

[21] A.P. Keil, J.L. Daniels, I. Hertz-Picciotto, Autism spectrum disorder, flea and tick medication, and adjustments for exposure misclassification: the CHARGE (childhood autism risks from genetics and environment) case-control study, Environ. Health 13 (1) (2014) 3.

[22] S.X. Ren, S.Y. Wang, Y.F. Liu, Y.X. Wang, F. Gao, Y.J. Dai, A review on current pollution and removal methods of tetracycline in soil, Sep. Sci. Technol. 58 (14) (2023) 2578–2602.

[23] S. Cui, J.L. Lv, R. Hough, Q. Fu, L.H. An, Z.L. Zhang, Y.X. Ke, Z.K. Liu, Y.-F. Li, Recent advances and prospects of neonicotinoid insecticides removal from aquatic environments using biochar: adsorption and degradation mechanisms, Sci. Total Environ. 939 (2024) 173509.

[24] Y.F. Ma, L. Wu, P. Li, L. Yang, L.Y. He, S.Y. Chen, Y.Y. Yang, F. Gao, X.B. Qi, Z. L. Zhang, A novel, efficient and sustainable magnetic sludge biochar modified by graphene oxide for environmental concentration imidacloprid removal, J. Hazard. Mater. 407 (2021) 124777.

[25] P. Zhang, X.H. Wang, B. Xue, P. Huang, Y.L. Hao, J.C. Tang, S.P. Maletic, S. D. Ronc̆evi`c, H.W. Sun, Preparation of graphite-like biochars derived from straw and newspaper based on ball-milling and TEMPO-mediated oxidation and their supersorption performances to imidacloprid and sulfadiazine, Chem. Eng. J. 411 (2021) 128502.

[26] J.Y. Tang, Y.F. Ma, C.Y. Zeng, L. Yang, S. Cui, S.L. Zhi, F.X. Yang, Y.Z. Ding, K. Q. Zhang, Z.L. Zhang, Fe-Al bimetallic oxides functionalized-biochar via ball milling for enhanced adsorption of tetracycline in water, Bioresour. Technol. 369 (2023) 128385.

[27] S. Cui, J.L. Lv, R. Hough, Q. Fu, Z.L. Zhang, X.L. Dong, X.H. Fan, Y.-F. Li, Imidacloprid removal by modified graphitic biochar with Fe/Zn bimetallic oxides, Environ. Res. 258 (2024) 119444.

[28] Q. Zhou, W.J. Mai, Z.G. Chen, X.Z. Wang, M.J. Pu, J. Tu, C. Zhang, X.H. Yi, M. Z. Huang, Thiamethoxam adsorption by $ZnCl_2$ modified cow manure biochar: mechanism and quantitative prediction, Environ. Res. 237 (2023) 117004.

[29] X.H. Wang, P. Zhang, C.P. Wang, H.Z. Jia, X.F. Shang, J.C. Tang, H.W. Sun, Metal-rich hyperaccumulator-derived biochar as an efficient persulfate activator: role of intrinsic metals (Fe, Mn and Zn) in regulating characteristics, performance and reaction mechanisms, J. Hazard. Mater. 424 (2022) 127225.

[30] D.J. Fu, H.J. Huang, H.T. Wang, M.Y. Ma, D. Qi, X.J. Lu, Characteristics and research progress of chitosan-modified biochar, J. Hainan Trop. Ocean Univ. 30 (05) (2023) 59–71.

[31] Y.Z. He, J. Ifthikar, L. Yang, Z.Q. Chen, Simultaneous elimination of vanadium(V) and sulfamethoxazole from livestock wastewater with nitrogen-impregnated biochar, J. Environ. Chem. Eng. 11 (2023) 111105.

[32] V. Son Tran, H. Hao Ngo, W.S. Guo, T. Ha Nguyen, T. Mai Ly Luong, X. Huan Nguyen, T. Lan Anh Phan, V. Trong Le, M. Phuong Nguyen, M. Khai Nguyen, New chitosan-biochar composite derived from agricultural waste for removing sulfamethoxazole antibiotics in water, Bioresour. Technol. 385 (2023) 129384.

[33] Y.Q. Sun, I.K.M. Yu, D.C.W. Tsang, J.J. Fan, J.H. Clark, G. Luo, S.C. Zhang, E. Khan, N.J.D. Graham, Tailored design of graphitic biochar for high-efficiency and chemical-free microwave-assisted removal of refractory organic contaminants, Chem. Eng. J. 398 (2020) 125505.

[34] R.A.K. Rao, S. Ikram, Sorption studies of Cu(II) on gooseberry fruit (emblica officinalis) and its removal from electroplating wastewater, Desalination 277 (1–3) (2011) 390–398.

[35] Y.X. Ke, F.X. Zhang, Z.L. Zhang, H. Rupert, Q. Fu, Y.-F. Li, S. Cui, Effect of combined aging treatment on biochar adsorption and speciation distribution for Cd (II), Sci. Total Environ. 867 (2023) 161593.

[36] K. Zhu, Q. Bin, Y. Shen, J. Huang, D. He, W. Chen, In-situ formed N-doped bamboolike carbon nanotubes encapsulated with Fe nanoparticles supported by biochar as highly efficient catalyst for activation of persulfate (PS) toward degradation of organic pollutants, Chem. Eng. J. 402 (2020) 126090.

[37] X.Z. Miao, X.L. Chen, W.H. Wu, D.H. Lin, K. Yang, Intrinsic defects enhanced biochar/peroxydisulfate oxidation capacity through electron-transfer regime, Chem. Eng. J. 438 (2022) 135606.

[38] Y.G. Abou El-Reash, M. Otto, I.M. Kenawy, A.M. Ouf, Adsorption of Cr(VI) and As (V) ions by modified magnetic chitosan chelating resin, Int. J. Biol. Macromol. 49 (2011) 513–522.

[39] S. Ahmad, F.L. Gao, H.H. Lyu, J.K. Ma, B.B. Zhao, S.Y. Xu, C. Ri, J.C. Tang, Temperature-dependent carbothermally reduced iron and nitrogen doped biochar composites for removal of hexavalent chromium and nitrobenzene, Chem. Eng. J. 450 (2022) 138006.

[40] V.N. Tsaneva, W. Kwapinski, X. Teng, B.A. Glowacki, Assessment of the structural evolution of carbons from microwave plasma natural gas reforming and biomass pyrolysis using Raman spectroscopy, Carbon 80 (2014) 617–628.

[41] P. Pradip, S. Dhanraj, M. Mainak, Q. Xu, Fabrication of carbon nanorods and graphene nanoribbons from a metal-organic framework, Nat. Chem. 8 (7) (2016) 718–724.

[42] Y.L. Mei, J. Xu, Y. Zhang, B. Li, S.S. Fan, H.C. Xu, Effect of Fe-N modification on the properties of biochars and their adsorption behavior on tetracycline removal from aqueous solution, Bioresour. Technol. 325 (2021) 124732.

[43] Y.F. Ma, T.M. Lu, J.Y. Tang, P. Li, O. Mašek, L. Yang, L. Wu, L.Y. He, Y.Z. Ding, F. Gao, X.B. Qi, Z.L. Zhang, One-pot hydrothermal synthesis of magnetic N-doped sludge biochar for efficient removal of tetracycline from various environmental waters, Sep. Purif. Technol. 297 (2022) 121426.

[44] Y.L. Chen, M. Hassan, M. Nuruzzaman, H.M. Zhang, R. Naidu, Y.J. Liu, L. Wang, Iron-modified biochar derived from sugarcane bagasse for adequate removal of aqueous imidacloprid: sorption mechanism study, Environ. Sci. Pollut. Res. 30 (2023) 4754–4768.

[45] Y.D. Chen, X.G. Duan, C.F. Zhang, S.B. Wang, N.Q. Ren, S.H. Ho, Graphitic biochar catalysts from anaerobic digestion sludge for nonradical degradation of micropollutants and disinfection, Chem. Eng. J. 384 (2020) 123244.

[46] Y. Wang, X. Zhou, L. Xiu, R. Shan, H.R. Yuan, Preparation of K_2FeO_4 modified biochar and its adsorption characteristics for Cd (II) in aqueous solution, Ecotox. Environ. Safe. 30 (2021) 2380–2386.

[47] J.L. Wang, M. Yuan, N.N. Cao, J.H. Zhu, J.W. Ji, D.S. Liu, R.M. Gao, S. Pang, Y. Q. Ma, In situ boron-doped cellulose-based biochar for effective removal of neonicotinoids: adsorption mechanism and safety evaluation, Int. J. Biol. Macromol. 237 (2023) 124186.

[48] Y.Y. Zou, Y. Yuan, T. Shen, Y. Zhou, Study on the adsorptive performance of imidacloprid from aqueous solution by $FeCl_3$ modified biochar derived from sludge, Acta Sci. Circumst. 41 (09) (2021) 3478–3486.

[49] L. Jiang, Y. Liu, S. Liu, X. Hu, G. Zeng, X. Hu, S. Liu, S. Liu, B. Huang, M. Li, Fabrication of β-cyclodextrin/poly (l-glutamic acid) supported magnetic graphene oxide and its adsorption behavior for 17β-estradiol, Chem. Eng. J. 308 (2017) 597–605.

[50] Y. Feng, G. Chen, Y. Zhang, D. Li, C. Ling, Q. Wang, G. Liu, Superhigh coadsorption of tetracycline and copper by the ultrathin g-C_3N_4 modified graphene oxide hydrogels, J. Hazard. Mater. 424 (2022) 127362.

[51] K. Li, Z. Zheng, Y. Li, Characterization and lead adsorption properties of activated carbons prepared from cotton stalk by one-step H_3PO_4 activation, J. Hazard. Mater. 181 (2010) 440–447.

[52] A. Wang, X. Hu, Y. Wan, G.G. Mahai, Y. Jiang, W.Q. Huo, X.G. Zhao, G.D. Liang, Z. Y. He, W. Xia, S.Q. Xu, A nationwide study of the occurrence and distribution of atrazine and its degradates in tap water and groundwater in China: assessment of human exposure potential, Chemosphere 252 (2020) 126533.

[53] R.-Z. Wang, D.-L. Huang, Y.-G. Liu, C. Zhang, C. Lai, X. Wang, G.-M. Zeng, Q. Zhang, X.-M. Gong, P. Xu, Synergistic removal of copper and tetracycline from aqueous solution by steam-activated bamboo-derived biochar, J. Hazard. Mater. 384 (2020) 121470.

[54] D.H. Ding, S.J. Yang, X.Y. Qian, L.W. Chen, T.M. Cai, Nitrogen-doping positively whilst sulfur-doping negatively affect the catalytic activity of biochar for the degradation of organic contaminant, Appl Catal B 263 (2020) 118348.

[55] L. Zhu, N. Zhao, L. Tong, Y.Z. Lv, G.J. Li, Characterization and evaluation of surface modified materials based on porous biochar and its adsorption properties for 2, 4-dichlorophenoxyacetic acid, Chemosphere 210 (2018) 734–744.

[56] X.T. Zhang, J.J. Hou, S.D. Zhang, T. Cai, S.J. Liu, W.J. Hu, Q.Z. Zhang, Standardization and micromechanistic study of tetracycline adsorption by biochar, Biochar 6 (2024) 12.

[57] R.T. Ji, Y.R. Wu, Y.R. Bian, Y. Song, Q. Sun, X. Jiang, L.J. Zhang, J.G. Han, H. Cheng, Nitrogen-doped porous biochar derived from marine algae for efficient solid-phase microextraction of chlorobenzenes from aqueous solution, J. Hazard. Mater. 407 (2021) 124785.

[58] L. Yan, Y. Liu, Y. Zhang, S. Liu, C. Wang, W. Chen, C. Liu, Z. Chen, Y. Zhang, $ZnCl_2$ modified biochar derived from aerobic granular sludge for developed microporosity and enhanced adsorption to tetracycline, Bioresour. Technol. 297 (2020) 122381.

[59] P. Zhang, H.W. Sun, C. Ren, L.J. Min, H.M. Zhang, Sorption mechanisms of neonicotinoids on biochars and the impact of deashing treatments on biochar structure and neonicotinoids sorption, Environ. Pollut. 234 (2018) 812–820.

[60] F. Wang, W. Sun, W. Pan, N. Xu, Adsorption of sulfamethoxazole and 17β- estradiol by carbon nanotubes/$CoFe_2O_4$ composites, Chem. Eng. J. 274 (2015) 17–29.

[61] S.Z. Li, Z.L. Zhang, C. Zhang, Y.T. He, X.H. Yi, Z.G. Chen, M.A. Hassaan, Ael. Nemr, M.Z. Huang, Novel hydrophilic straw biochar for the adsorption of neonicotinoids: kinetics, thermodynamics, influencing factors, and reuse performance, Environ. Sci. Pollut. Res. 30 (2023) 29143–29153.

[62] T.B. Nguyen, Q.M. Truong, C.W. Chen, R.A. Doong, W.H. Chen, C.D. Dong, Mesoporous and adsorption behavior of algal biochar prepared via sequential hydrothermal carbonization and $ZnCl_2$ activation, Bioresour. Technol. 346 (2022) 126351.

[63] H. Zhang, Z. Wang, J. Gao, J. Zhu, C. Xie, X. Xie, Adsorption characteristics of norfloxacin by biochars derived from reed straw and municipal sludge, Environ. Sci. 37 (2016) 689–696.

[64] B. Wang, Y. Jiang, F. Li, D. Yang, Preparation of biochar by simultaneous carbonization, magnetization and activation for norfloxacin removal in water, Bioresour. Technol. 233 (2017) 159–165.

[65] J. Liu, X. Kang, X. He, P. Wei, Y. Wen, X. Li, Temperature-directed synthesis of N doped carbon-based nanotubes and nanosheets decorated with Fe (Fe_3O_4, Fe_3C) nanomaterials, Nanoscale 11 (18) (2019) 9155–9162.

[66] P.S. Pauletto, S.F. Lütke, G.L. Dotto, N.P.G. Salau, Adsorption mechanisms of single and simultaneous removal of pharmaceutical compounds onto activated carbon: isotherm and thermodynamic modeling, J. Mol. Liq. 336 (2021) 116203.

[67] L.H. Jiang, Y.G. Liu, G.M. Zeng, F.Y. Xiao, X.-J. Hu, X. Hu, H. Wang, T.-T. Li, L. Zhou, X.-F. Tan, Removal of 17 beta-estradiol by few-layered graphene oxide

nanosheets from aqueous solutions: external influence and adsorption mechanism, Chem. Eng. J. 284 (2016) 93–102.

[68] S. Zhang, T. Shao, S.S.K. Bekaroglu, T. Karanfil, Adsorption of synthetic organic chemicals by carbon nanotubes: effects of background solution chemistry, Water Res. 44 (2010) 2067–2074.

[69] J. Han, W. Qiu, Z. Cao, J. Hu, W. Gao, Adsorption of ethinylestradiol (EE2) on polyamide 612: molecular modeling and effects of water chemistry, Water Res. 47 (2013) 2273–2284.

[70] Y.J. Xiang, Z. Xu, Y.Y. Wei, Y.Y. Zhou, X. Yang, Y. Yang, J. Yang, J.C. Zhang, L. Luo, Z. Zhou, Carbon-based materials as adsorbent for antibiotics removal: mechanisms and influencing factors, J. Enviro. Manage. 237 (2019) 128–138.

[71] Z.J. Luo, X. Peng, W.W. Liang, D. Zhou, C.X. Dang, W.Q. Cai, Enhanced adsorption of roxarsone on iron–nitrogen co-doped biochar from peanut shell: synthesis, performance and mechanism, Bioresour. Technol. 388 (2023) 129762.

[72] Y.J. Dai, N.X. Zhang, C.M. Xing, Q.X. Cui, Q.Y. Sun, The adsorption, regeneration and engineering applications of biochar for removal organic pollutants: a review, Chemosphere 223 (2019) 12–27.

[73] X. Dong, G. Liu, F. Zhang, X. Fan, J. Lv, Q. Fu, S. Cui, Interlayer-expanded LDH@ biochar nanoreactors via sodium citrate mediation: unlocking hidden active sites for persulfate-driven imidacloprid removal, Environ. Chem. Ecotoxicol. 7 (2025) 1130–1141.

[74] X.H. Fan, Q. Fu, G.R. Liu, H.L. Jia, X.L. Dong, Y.-F. Li, S. Cui, Applying molecular oxygen for organic pollutant degradation: strategies, mechanisms, and perspectives, Environ. Sci. Ecotechnol. 22 (2024) 100469.

[75] L. Sellaoui, A. G`omez-Avil`es, F. Dhaouadi, J. Bedia, A. Bonilla-Petriciolet, S. Rtimi, C. Belver, Adsorption of emerging pollutants on lignin-based activated carbon: analysis of adsorption mechanism via characterization, kinetics and equilibrium studies, Chem. Eng. J. 452 (2023) 139399.

[76] X.L. Dong, Q. Fu, G.R. Liu, X.H. Fan, F.X. Zhang, Y.-F. Li, S. Cui, Imidacloprid degradation activated by peroxydisulfate with NiCoAl layered metal oxide catalysts: the unique role of Al, Sep. Purif. Technol. 356 (2024) 129845.

[77] I. Chataigner, C. Panel, H. Gérardb, S.R. Piettre, Sulfonylvs carbonyl group: which is the more electron-withdrawing? Chem. Commun. (2007) 3288–3290.

[78] J. Lalley, C. Han, X. Li, D.D. Dionysiou, M.N. Nadagouda, Phosphate adsorption using modified iron oxide-based sorbents in lake water: kinetics, equilibrium, and column tests, Chem. Eng. J. 284 (2016) 1386–1396.